OPEN ACCESS
IOP Publishing | International Atomic Energy Agency Nuclear Fusion
Nucl. Fusion **62** (2022) 066035 (11pp) https://doi.org/10.1088/1741-4326/ac6072

Edge transport and fuelling studies via gas puff modulation in ASDEX Upgrade L-mode plasmas

C.U. Schuster[1,2,*], E. Wolfrum[1], E. Fable[1], R. Fischer[1], M. Griener[1], B. Tal[1], C. Angioni[1], T. Eich[1], P. Manz[3], U. Stroth[1,2] and the ASDEX Upgrade Team[a]

[1] Max-Planck-Institute for Plasma Physics, Garching, Germany
[2] Department of Physics E28, Technical University of Munich, Garching, Germany
[3] Institute of Physics, University of Greifswald, Greifswald, Germany

E-mail: christian.schuster@ipp.mpg.de

Received 17 December 2021, revised 16 March 2022
Accepted for publication 23 March 2022
Published 14 April 2022

Abstract

Gas puff modulation experiments are performed at ASDEX Upgrade in L-mode plasmas. We model the discharge with the ASTRA transport code in order to determine transport coefficients outside of a normalized radius of $\rho_{\mathrm{pol}} = 0.95$. The experimental data is consistent with a range of particle diffusivities and pinch velocities of the order of $D = (0.20 \pm 0.13)\ \mathrm{m^2\ s^{-1}}$ and $v = (-1 \pm 2)\ \mathrm{m\ s^{-1}}$, respectively. The electron temperature response caused by the gas modulation permits to estimate also that heat diffusivity χ_{e} increases almost linearly when collisionality rises due to fuelling. The fuelling particle flux is amplified by recycling, overcompensating losses.

Keywords: particle transport, turbulence, neutral recycling, transport coefficients, pinch, tokamak, plasma

(Some figures may appear in colour only in the online journal)

1. Introduction

The density and temperature profiles just inside of the separatrix are crucial for most edge phenomena. Additionally, they set the boundary conditions for core temperatures and densities, and thus fusion performance [1–3]. Without knowledge about the mechanisms determining these profiles it is not possible to predict the performance of future devices.

Our main focus is the density profile. It is determined by the particle source from ionized neutral atoms, and particle transport with diffusive and convective contributions. Inward convective transport is referred to as pinch. In the core plasma the particle source is negligible or well quantifiable in most scenarios, simplifying the analysis considerably. Situations where the density profile is evolving, e.g. because the fuelling gas flow is modulated, can then be used to separate particle diffusion from convection [4–9]. Disentangling the individual contributions is more challenging at the plasma edge because neutral atoms crossing the separatrix result in a particle source which is difficult to quantify. One approach is then to compare different discharges with variations in density, and therefore the neutral penetration, and compare the shape of the edge density profiles to each other and to theoretical predictions [10–13]. Another approach to directly determine the individual contributions is to study evolving plasma states, and include the particle source in the analysis [14].

In this work we follow the latter approach and perturb the plasma using a fast switching gas valve [15]. We then use the transport code ASTRA [16–18] to model the kinetic profiles

* Author to whom any correspondence should be addressed.
[a] See Meyer *et al* 2019 (https://doi.org/10.1088/1741-4326/ab18b8) for the ASDEX Upgrade Team.

and determine the transport coefficients. ASTRA is 1.5 dimensional, meaning the transport equations are one dimensional because the quantities are assumed to be in equilibrium on each flux surface, and the geometry is treated two dimensionally.

We not only analyse the evolution of the electron density n_e but also the electron temperature T_e. Including T_e allows us to show that transport itself is perturbed by the modulation, rendering the common assumption of temporally constant transport coefficients incorrect. By virtue of the well resolved measurements of n_e and T_e we can nevertheless determine particle transport coefficients, and quantify the modulation of the heat diffusivity χ_e. The modulation of χ_e correlates well with a modulation of the collisionality ν^*, as predicted by theory [19–22]. Of particular interest for us is the predicted linear relationship between χ_e and ν^* for drift-Alfvén turbulence [23].

We start with an introduction to the experimental setup. This is followed by a presentation and discussion of the measured data, where already first conclusions about particle transport will be extracted from the data. Thereafter we model the discharge with ASTRA and infer transport properties. We end by collecting the main results.

2. Experimental setup and measurements

For our transport analysis the plasma is perturbed by modulating the gas flow into the vacuum vessel utilizing fast acting valves [15]. Transitioning from zero to full fuelling takes less than 1 ms. The fuelling rate is 8×10^{21} deuterium atoms per second (120 Torr L s^{-1}) with a modulation frequency of 25 Hz, giving a modulation period of 40 ms. The valve opens at $t = 0$ and closes at $t = 22$ ms. The valve, which was characterized by Griener *et al* [15], is located at the outer midplane.

All experimental data is from L-mode discharge #37758 in the tokamak ASDEX Upgrade (AUG) [24] with a plasma current of $I_P = 0.8$ MA and a toroidal magnetic field of $B_t = -2.4$ T. Central electron cyclotron resonance heating of 590 kW is applied in addition to Ohmic heating of 440 kW, while the radiation losses are about 200 kW [25]. In figure 1 we show selected quantities for the discharge under investigation. The stored energy W_{mhd} (figure 1(*a*)) remains constant except for experimental noise, while the electron temperature (figure 1(*b*)) and the line integrated electron density (figures 1(*c*) and (*d*)) oscillate with the fuelling modulation around a constant background. In the following we will investigate the measured modulation in detail, we average over the nine modulation periods to obtain a more accurate mean response and the standard deviation thereof.

Edge density. The density modulation and its temporal evolution are clearly visible in interferometry [26] measurements. In figure 2 we show the core channel H1 and the edge channel H5 (tangential to the flux surfaces at a normalized minor radius of $\rho_{pol} = 0.21$ and $\rho_{pol} = 0.88$ respectively). The other channels behave analogously and are not shown to avoid clutter. While we show the full signal in figure 2(*a*) we subtract the mean to highlight the modulation in figure 2(*b*). After the valve is opened the density increases, it decreases again when the valve is closed. Until $t \approx 9$ ms the density

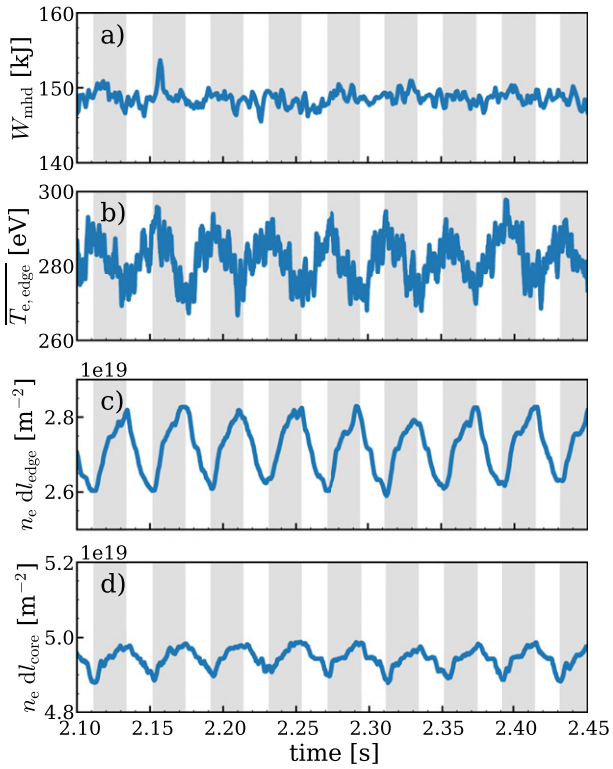

Figure 1. Overview of the discharge segment under investigation. The fuelling valve is open in the grey shaded intervals, and closed in the unshaded intervals. We show the stored energy (*a*), the average electron temperature as measured by ECE channels between $\rho_{pol} = 0.8$ and $\rho_{pol} = 0.9$ (*b*), and the line integrated density from the interferometry edge channel H5 (*c*) and the core channel H1 (*d*).

increase is steeper than afterwards. The modulation is dominated by the plasma inside the separatrix because the measured SOL modulation of $\approx \pm 2 \times 10^{18}$ m^{-3} integrated over few centimeters is small compared to the modulation amplitude of $\approx \pm 1 \times 10^{18}$ m^{-2}. We will nevertheless include the SOL effect later during modelling. Already without modelling we can conclude that the modulation mainly comes from the plasma edge: when we assume that the modulation measured by the edge channel is exclusively due to a uniform density modulation between $\rho_{pol} = 0.9$ and $\rho_{pol} = 1.0$ we would expect the red dotted line as signal for the core channel. Because the red dotted line agrees well with the measured signal from the core channel we conclude that the density modulation is, mostly, localized outside of $\rho_{pol} = 0.9$. When modelling the discharge we will integrate the density accurately and not rely on such assumptions.

Outside of $\rho_{pol} \approx 0.985$ the lithium [27, 28] and thermal helium beam [29, 30] diagnostics measure the density modulation temporally and spatially resolved. The profiles are shown in figures 3(*a*) and (*b*). The SOL density increases strongest, with diminishing increases towards the core plasma: while the separatrix density still increases this is not the case at $\rho_{pol} = 0.99$. As a result the separatrix density gradient flattens by 8% (lithium beam) or 9% (helium beam) when the valve opens. Unless an increase in fuelling leads to less particle flux

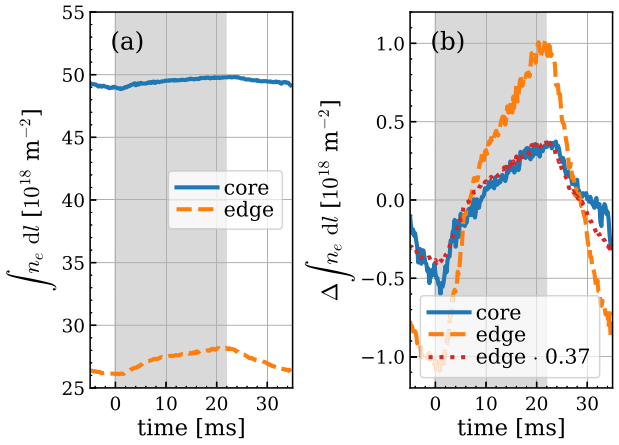

Figure 2. Interferometry channels H1 (core) and H5 (edge), conditionally averaged. In the grey shaded intervals the fuelling valve is open, and closed otherwise. We show the full signals (*a*) and the signals with the mean subtracted (*b*). The red dotted line is the signal one would expect if only plasma outside of $\rho_{\mathrm{pol}} = 0.9$ modulates.

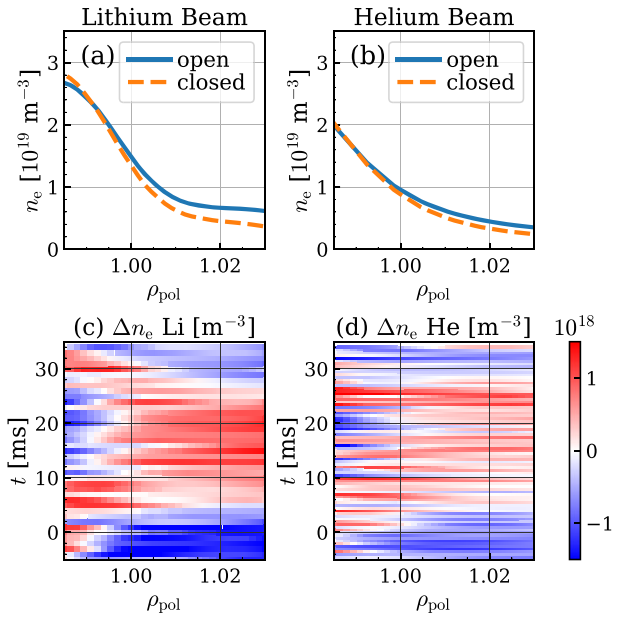

Figure 3. Edge density profiles from the lithium beam (*a*) and the thermal helium beam (*b*) in the equilibrated phase before the valve opens (−5 ms to 0 ms, dashed orange line) and the equilibrated phase just before the valve closes (15 ms to 20 ms, solid blue line). The temporal evolution is shown in (*c*) for the lithium beam and in (*d*) for the thermal helium beam.

this shows that more particles are transported with a shallower gradient, suggesting an increase in transport or a change of the profile shape due to local ionization.

The temporal evolution is shown in figures 3.(*c*) and (*d*) After the valve is opened at $t = 0$ density increases with a delay of about 3 ms. The gradient flattens at $t \approx 10$ ms, visible in the lithium beam data as a change from red to blue in the confined region. Meanwhile the SOL density remains high. According to the lithium beam data the density relaxes back to

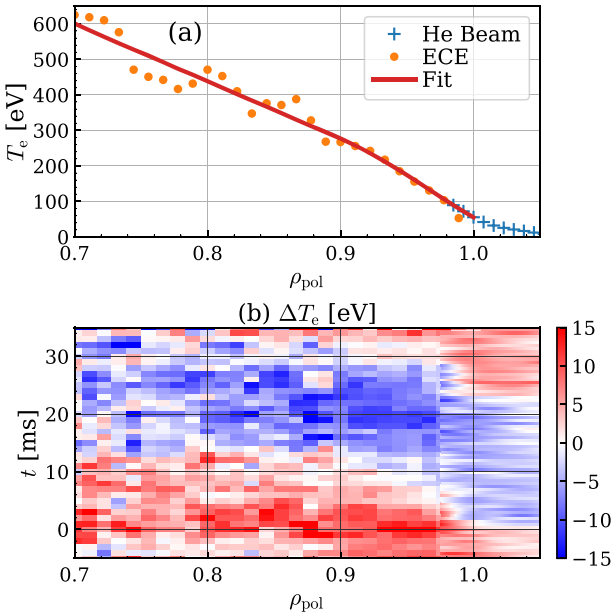

Figure 4. The electron temperature profile from ECE and thermal helium beam diagnostics, with the fit used in modelling (*a*), and the temporal evolution of T_e (*b*).

the state before the valve was opened after the valve closes at $t = 22$ ms, again with a delay of ≈3 ms. The helium beam shows an increase in density at $t = 22$ ms, which appears to be a diagnostic artefact as the electron temperature increases simultaneously.

Electron temperature: ECE and thermal helium beam. In figure 4 we show the electron temperature profile and its temporal evolution outside of $\rho_{\mathrm{pol}} = 0.7$. The electron temperature further inside does not influence our edge transport studies, and the temporal evolution is dominated by saw-tooth activity. The ECE is optically thick until $\rho_{\mathrm{pol}} = 0.965$, resulting in reliable T_e measurements. Further outside the thermal helium beam is able to measure the temperature profile, the modulation amplitude and the modulation phase, and agrees well with the ECE diagnostic.

After the valve is opened at $t = 0$ the temperature in the SOL drops by ≈10 eV over 3 ms, and recovers on the same time scale after the valve is closed. This perturbation continues in the confined region as a cold pulse. By fitting a sine at every radial position to the electron temperature we obtain the amplitude and phase of the modulation, which are shown in figure 5. Note that in this work we define the amplitude as the prefactor of the sine, therefore a modulation amplitude of 1 eV corresponds to a difference between minimum and maximum of 2 eV. Starting from the separatrix with ±7 eV the amplitude of the cold pulse increases strongly and peaks at $\rho_{\mathrm{pol}} \approx 0.92$ at ±11 eV. Going further inwards the amplitude decays to ±5 eV at $\rho_{\mathrm{pol}} = 0.7$. The phase delay increases when moving inwards, starting at 2.5 ms. Initially the propagation speed is comparably slow (large time difference for small change in ρ_{pol}), with the delay increasing to 9 ms at $\rho_{\mathrm{pol}} = 0.98$. Then, the propagation speeds up, reaching $\rho_{\mathrm{pol}} = 0.7$ with a total delay of 14 ms. Noise, both on the profile and the temporal evolution,

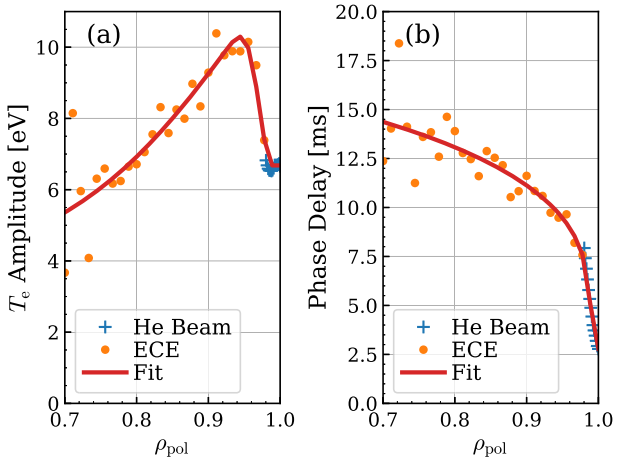

Figure 5. Amplitude (*a*) and phase (*b*) of the electron temperature modulation as measured by ECE (orange circles) and the thermal helium beam (blue crosses). Additionally we show the fits used in modelling in red.

disturbs the transport analysis we will perform in section 3. We therefore remove the noise by using the red fits shown in figures 4 and 5 instead of the raw data.

3. Modelling

We use the 1.5D transport code ASTRA to model the plasma profiles in realistic geometry. The profiles are evolved according to the transport equations

$$\frac{\partial n_e}{\partial t} = \frac{\partial}{\partial \rho}\left(D\frac{\partial n_e}{\partial \rho} - v n_e\right) + S_e \tag{1}$$

$$\frac{3}{2}\frac{\partial (n_e T_e)}{\partial t} = \frac{\partial}{\partial \rho}\left(n_e \chi_e \frac{\partial T_e}{\partial \rho}\right) + P_e \tag{2}$$

$$\frac{3}{2}\frac{\partial (n_i T_i)}{\partial t} = \frac{\partial}{\partial \rho}\left(n_i \chi_i \frac{\partial T_i}{\partial \rho}\right) + P_i, \tag{3}$$

where we omit geometrical factors which are given elsewhere [16]. n_e is the electron density, $n_i \approx n_e/Z_{eff}$ the ion density with $Z_{eff} = 1.2$, ρ the normalized flux coordinate, S_e the electron particle source, P_e the power density heating the electrons, and P_i the power density heating the ions. The interaction between neutral atoms and the plasma occurs through S_e, P_e and P_i.

The transport coefficients in equations (1)–(3) are not necessarily constant, but are allowed to change as function of time or of plasma parameters. We modelled the discharge with constant transport coefficients and additional off-diagonal terms such as thermodiffusion, but reproducing both the temperature profile and the cold pulse propagation was only possible by allowing an evolving χ_e. With χ_e not being temporally constant, the experimental data does not allow to draw conclusions about the off-diagonal terms, which we will therefore not consider in the following.

Another aspect to be discussed is the description of transport as diffusive and convective. This assumption is well-founded if the transport exhibits Gaussian statistics [31], what is the case close to the separatrix [32, 33]. Perpendicular transport in the SOL on the other hand is dominated by large intermittent filaments [34, 35]. But even though this intermittent transport is not Gaussian, we can describe it as diffusive on the comparably long millisecond time scale we are investigating [36]. We can therefore expect that our description of transport with equations (1)–(3) is valid, even if intermittent contributions from filaments are present.

We simulate 50 periods to equilibrate, resulting in a simulated time of 2 s, and take data from the last period. In the following we describe the setup for the transport coefficients and source terms in equations (1)–(3). Because many quantities appearing in the transport equations are not known *a priori* we have to introduce several unknown parameters. The treatment of these parameters will be discussed in section 4.

Particle transport. We use the lithium beam data for $\rho_{pol} > 0.99$, further inside we perform predictive simulation as for T_i. We prescribe the transport coefficients D and v and predict the resulting density profile and its evolution. Previously, when discussing figure 3, we found indications that the particle transport might evolve with time. To investigate how strongly our analysis is influenced by this uncertainty we consider two different cases: a temporally constant D and a D that modulates outside of $\rho_{pol} = 0.95$. Phase and amplitude of the D modulation are two parameters of our model.

We cannot determine whether a nonzero pinch velocity v exists in the plasma edge, as will become apparent when discussing the results. We will therefore not investigate a temporal evolution of v, as this would be a comparably small change in a poorly determined quantity, and keep v constant. We prescribe piece wise constant profiles with jumps at $\rho_{pol} = [0.5, 0.7, 0.95]$ for the particle transport coefficients. We position these jumps to coincide with abrupt changes in the gradients of the experimental profiles. These positions are therefore not universal for L-modes in general but depend on the analysed discharges. The outer position $\rho_{pol} = 0.95$, which is the only one relevant for our edge transport studies, is however typical for AUG L-modes. Inside of $\rho_{pol} = 0.7$ we only fit the ratio of D and v because we cannot disentangle them for a lack of experimental data showing the modulation. We impose a nonpositive pinch velocity for $\rho_{pol} < 0.7$ to avoid hollow profiles.

Neutral population and particle source. We have no measurements of the flux-surface averaged neutral particle density or its temporal evolution, therefore we parameterize and vary it. With ASTRA we can calculate the neutral density profile for a given separatrix density and a given ratio between cold and hot neutrals, which we define to have 2 eV for Franck–Condon neutrals and 25 eV for neutrals that underwent charge exchange in the SOL. For solving the Fokker–Planck equation describing the neutral population ASTRA uses slab geometry, which cannot capture the effect of different flux expansions which would lead to wider or narrower neutral density profiles. But because we vary the ratio of cold and hot neutrals, which also influences the width of the neutral density profile, we indirectly include the effects of the fuelling position and flux expansion when varying the energy distribution of the neutrals at the separatrix. Analogously,

an altered source profile due to turbulent fluctuations as calculated by Marandet *et al* [37], is described in an integral way by the flexible width of our particle source.

The neutral population interacts with the plasma according to ionization and charge exchange cross sections and rate coefficients: an electron impact ionization leads to a loss of 13.6 eV in the electron channel and the gain of the neutral energy in the ion channel. A charge exchange reaction leads to the loss of thermal ion energy and the gain of the original neutral energy in the ion channel.

The neutral population, and therefore the source term, are parametrized as follows: in addition to the ratio between cold and hot neutrals, and the separatrix neutral densities in the phases with open and closed valve, we have two parameters for the timing of the neutrals: the delay between the valve opening and the change in neutral density, and the temporal width of the linear transition between the open and closed state.

Power terms. Electrons receive power from Ohmic and (central) ECR heating, and are cooled by radiation, collisional heat transfer to ions, and ionizing and exciting neutral atoms. The contributions of neutrals are much smaller than the other terms, but as they are directly influenced by the gas puff modulation we include them to avoid attributing changes to altered transport when they actually stem from neutral interactions. Ions are only heated by collisional heat exchange, and cooled by charge exchange reactions with cold neutrals. Recombination of ions and electrons also removes heat from the ion channel. Although this last contribution is very small we include it as it does not complicate the analysis. We select the tungsten concentration such that the radiated power matches the experiment.

Heat transport. For T_e we have accurate measurements for the whole domain. We therefore can prescribe the experimental profile and its temporal evolution. As we know the power fluxes and ∇T_e we can calculate the electron heat diffusivity χ_e needed to arrive at the experimental T_e. For T_i on the other hand there are no measurements available. We therefore assume $T_\mathrm{e} = T_\mathrm{i}$ at $\rho_\mathrm{pol} > 0.99$, which is realistic for L-modes with moderately high density such as the discharge analysed here. To correctly predict the heat fluxes we need T_i in the whole plasma. We thus set $\chi_\mathrm{i} \propto \chi_\mathrm{e}$ with an undetermined proportionality constant.

Upper bound for particle flux due to energy considerations. Each neutral atom that is ionized results in a cold electron and a cold ion that have to be heated up to local plasma temperatures, in addition to the comparably little 13.6 eV required for ionization. This power for heating up freshly ionized particles is kept track of indirectly: in the long term, every electron and every ion that was added to the plasma leaves the plasma again and takes thermal energy with it, resulting in outward convective heat fluxes. In most works, including this work, these convective heat fluxes do not appear explicitly in equations (2) and (3). Instead these losses are included implicitly in χ_e and χ_i. This however can hide the following issue: with large particle fluxes the convective heat fluxes could become larger than the heating power entering the plasma. The turbulent heat conduction would then have to be negative to transport power from the outer plasma boundary inward, from low to high temperatures.

In this section we describe how we detect such unphysical situations. We calculate the power needed to ionize and heat all particles entering the main plasma. If this power exceeds the total heating power we discard the simulation.

The speed of the neutral particle before ionization is negligible when considering the energy required for heating up the electron, but not for the ion. With $Z_\mathrm{eff} \approx 1$ the particle fluxes of electrons, ions, and neutrals have to be equal in absolute value for the ionization process: $\Gamma_\mathrm{e} = \Gamma_\mathrm{i} = \Gamma_\mathrm{n}$.

$$P_\mathrm{heatup,\,e} = \frac{3}{2} T_\mathrm{e} \Gamma_\mathrm{n} \tag{4}$$

$$P_\mathrm{heatup,\,i} = \frac{3}{2} \left(T_\mathrm{i} - T_\mathrm{n}\right) \Gamma_\mathrm{n} \tag{5}$$

$$P_\mathrm{ion} = 13.6\ \mathrm{eV} \cdot \Gamma_\mathrm{n} \tag{6}$$

$$P_\mathrm{loss,\,tot} = P_\mathrm{heatup,\,e} + P_\mathrm{heatup,\,i} + P_\mathrm{ion} \tag{7}$$

$$= \left(\frac{3}{2}\left(T_\mathrm{e} + T_\mathrm{i} - T_\mathrm{n}\right) + 13.6\ \mathrm{eV}\right) \Gamma_\mathrm{n}. \tag{8}$$

We exclude all results where $P_\mathrm{loss,\,tot} > 1.2\,(P_\mathrm{heat} - P_\mathrm{rad}) \approx 1.2{\cdot}830$ kW, where we include a tolerance of 20% to account for uncertainties.

4. Fitting and inference

In this section we discuss how we determine values for the free parameters such that simulation and experiment are in agreement. The most complete treatment would be to sample the parameter space extensively and use Bayesian inference to determine the probability distribution of the physical coefficients. Using the common Markov chain Monte Carlo (MCMC) sampling scheme one would directly get points in parameter space distributed according to the sought-after probability distribution. Unfortunately a single ASTRA run has a runtime of several minutes, making standard sampling schemes for Bayesian inference unfeasible. Instead we take a different approach: starting from random initial parameters we optimize the parameters for good agreement with the experiment. By repeating this procedure several times we obtain a set of solutions. Due to local minima and a finite number optimization steps the different fits will not converge to a single point. This set does not exactly correspond to the probability distribution of the parameters as a set obtained by MCMC sampling would. It however still allows us to judge which range of parameters result in agreement with the experiment, and are therefore plausible physical values. Just as with MCMC sampling we will interpret our samples in a statistical sense: isolated samples in good agreement with the experiment do not mean that they must lie within the uncertainty interval. Because they are few they correspond to a small volume of parameter space and are interpreted as lying in the tail of the probability distribution.

First of all we quantify the agreement with the experiment. The comparison between experiment and simulation is performed with the normalized mean squared error:

$$\chi^2 = \frac{1}{N}\sum_i \frac{\left(f_{i,\mathrm{ASTRA}} - f_{i,\mathrm{exp}}\right)^2}{\sigma_i^2}, \tag{9}$$

with N being the number of data points, $f_{i,\mathrm{exp}}$ the measured data, $f_{i,\mathrm{ASTRA}}$ the corresponding simulation result, and σ_i the experimental uncertainty. The experimental interferometry signal is compared with the signal of a virtual diagnostic which integrates n_e from ASTRA along the experimental measurement line. In the SOL, which ASTRA does not model, we take the lithium beam measurements and assume poloidal symmetry. Usually one normalizes not directly by N, but subtracts one plus the number of fitted parameters [38]. The different normalization only has a minor influence on χ^2 because the number of free parameters (12) is small compared to the number of fitted data points (112). The uncertainties σ_i for interferometry, which we can only estimate because of the poloidally unknown SOL density modulation, are far more influential. Because of the unknown SOL density response we will manually select a χ^2 threshold. This selection eliminates any influence the normalization would have.

We discriminate between systematic uncertainties, such as calibration errors, and statistical uncertainties, i.e. noise, by treating the temporal mean and the modulation as separate data points. The mean is normalized by the systematic error and the modulation by the statistical error. For the systematic error of interferometry we use the same values as the Bayesian integrated data analysis at AUG [39]: 2% for the three inner lines of sight, and 5% for the two outer channels. The statistical error we can determine directly from our measurement as described in section 2. However, there is a time dependent systematic error that we have to account for: the SOL density evolution might not be poloidally symmetric. We therefore add the influence of the SOL on the modulation in the interferometry signal, which we estimated in section 2, to the uncertainty.

We perform a maximum likelihood fit of the parameters, equivalent to minimizing χ^2. For the optimization itself we use a Gauss–Newton method with trust regions as implemented in the SciPy library in `scipy.optimize.least_squares` [40]. The parameters and the ranges within they are uniformly random initialized are given in table 1. Note that during the optimization the parameters may leave the ranges for their initial values.

The proportionality constant between χ_e and χ_i is special in that it does not influence any measured quantity directly. Therefore we do not fit it but instead keep it at the random initial value throughout the optimization procedure. The proportionality constant lies in $[0.05, 2]$. Similarly we will keep the amplitude (up to $\pm 30\%$) and phase of the D modulation constant at a random value to test the robustness of our results.

The final step to take before we can discuss results is to determine what values for χ^2 can be considered as in agreement with the experiment, and which values are too high to be considered acceptable. In principle we could use the obtained χ^2 value together with the χ^2 distribution [41, 1.3.6.6.6] to calculate the probability that the discrepancies between fit and measurement arise from measurement uncertainties. In practice this would require that the uncertainties σ_i in equation (9) are determined very accurately. We therefore additionally consider the two example fits shown in figure 6 with different χ^2 values to judge which fits to accept.

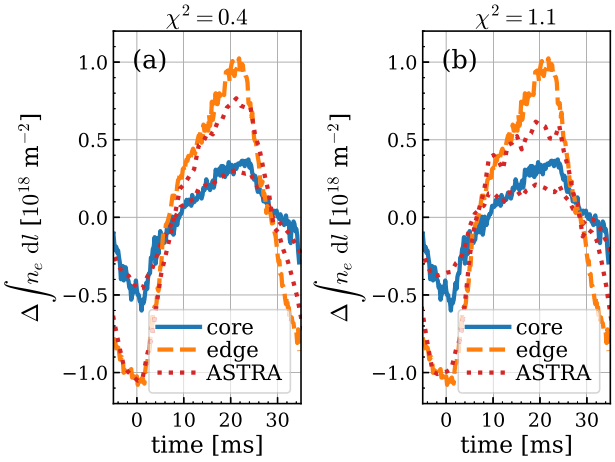

Figure 6. The density modulation as measured by interferometry channels H-1 (core) and H-5 (edge), and the simulated time traces from ASTRA. In (*a*) we show a fit with $\chi^2 = 0.4$, with modulating D, no pinch, and a mean neutral atom influx across the separatrix of $11 \times 10^{21}\ \mathrm{s}^{-1}$. The fit in (*b*) has $\chi^2 = 1.1$, with a temporally constant D, a pinch with $v = -13\ \mathrm{m\ s}^{-1}$, and a mean neutral atom influx across the separatrix of $6 \times 10^{21}\ \mathrm{s}^{-1}$.

For $\chi^2 = 0.4$ (figure 6(*a*)) the experimental time traces are fitted well. Some discrepancies are visible: the minimal and maximal values for H-5 are lower in the simulation than in the experiment, and while the simulated H-5 signal drops more slowly than the experimental one after $t = 30$ ms the H-1 signal drops faster. These discrepancies could however be caused by a non symmetric SOL behaviour or to some extent be statistical fluctuations. For $\chi^2 = 1.1$ (figure 6(*b*)) we find far more severe discrepancies: both for H-1 and H-5 the density reaches a steady state too early, resulting in too low densities at $t \approx 20$ ms. We select $\chi^2 = 1$ as threshold beyond which we do not plot the fits because the agreement is too poor.

5. Results

In this section we will investigate which particle diffusivities (D) and pinch velocities (v) can explain the density modulation measured in the experiment; we will see how the heat diffusivity χ_e evolves during the modulation; and which conclusions we can draw about the neutrals.

Figures 7–9 show the most important parameters from the successful simulations as function of the averaged neutral particle flux. The dependence of the determined quantities on the neutral particle flux is generally weak, with the pinch velocity v showing the strongest dependence. The minor variations in the determined quantities show the robustness of the results against variations in the unknown neutral particle flux.

Table 1. The 15 free parameters in the ASTRA model and the values they are initialized with. The last three are kept constant throughout the simulation to show that the results are insensitive to them.

Quantity	No. of scalar parameters	Initialization value or range
D	4	0.4 m^2 s^{-1} to 2 m^2 s^{-1}
v	2	-5 m s^{-1} to 5 m s^{-1}
Valve opening delay	1	3 ms
Valve transition time	1	3 ms
Tungsten concentration	1	5.5×10^{-6}
Share of cold neutrals at separatrix	1	90%
Neutral densities for open and closed valve	2	0.5×10^{16} m^{-3} to 4×10^{16} m^{-3}
Phase of D modulation	1 (fixed)	0 ms to 40 ms
Amplitude of D modulation	1 (fixed)	$\pm$0% to $\pm$30%
Proportionality constant between χ_e and χ_i	1 (fixed)	5% to 200%

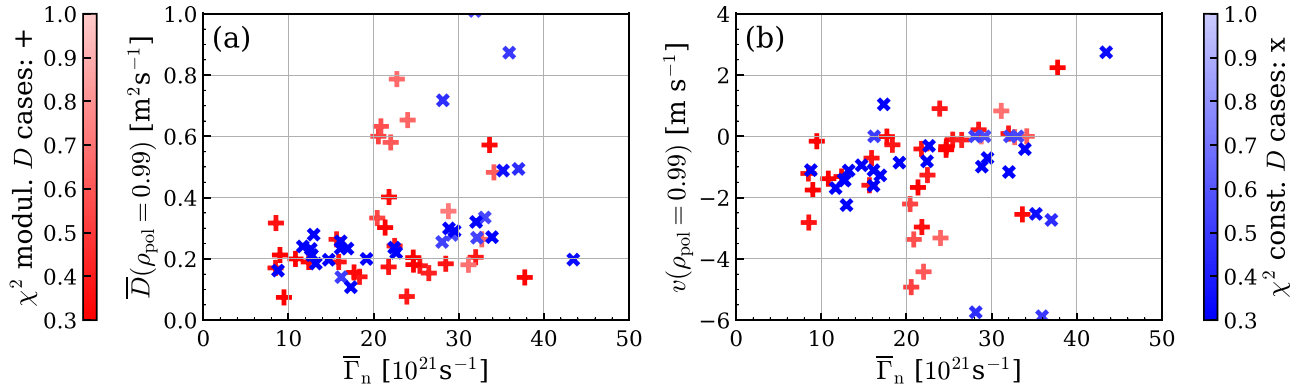

Figure 7. The mean particle diffusivity (a) and pinch velocity (b) at $\rho_{pol} = 0.99$, against the mean particle flux across the separatrix $\overline{\Gamma_n}$. Simulations utilizing modulating D appear as red $+$, simulations with temporally constant D as blue $\times$. There are isolated simulations with $\chi^2 > 0.7$ outside of the shown areas.

Points marked as red '+' correspond to simulations where D modulates between $\rho_{pol} = 0.95$ and $\rho_{pol} = 1$, while simulations that employ temporally constant D appear as blue '$\times$'. Only data points that are better than the threshold of $\chi^2 = 1$ we defined earlier are shown, with faint colours corresponding to high χ^2 values. Simulations with mean particle fluxes across the separatrix higher than $\approx 45 \times 10^{21}$ s^{-1} violate energy conservation, as described in section 3, and are therefore excluded.

Particle transport coefficients D and v. Figures 7(a) and (b) show the solution sets for D and v. Because D is time dependent in the modulating case (blue) we consider the temporal average $\overline{D}$. Most simulations are contained in $\overline{D} = (0.20 \pm 0.13)$ m^2 s^{-1} and $v = (-1 \pm 2)$ m s^{-1}. There are simulations with higher particle diffusivity and more negative pinch velocities, correlating with larger χ^2 values and worse agreement with the experiment. Red and blue crosses, corresponding to solutions of the two different transport models with constant and modulating D, are largely intermixed and do not occupy different regions in the parameter space.

Inference of neutral properties. The source profile and its temporal evolution are free parameters for the fitting routine (see section 3). We fit no measurements of neutrals, but because the temporal evolution of the interferometry time traces has to be reproduced it is nevertheless possible to draw some conclusions about the particle source. Figure 8(a) shows the share of cold 2 eV neutral atoms of all neutral atoms crossing the separatrix. The simulations cluster at high values: most simulations lie above 90%. This results in narrow source profiles. In the experiment this could also be due to fuelling in the vincinity of the X-point because of flux expansion besides low energies of neutral particles.

In figure 8(b) we show the difference in neutral atom flux across the separatrix for the open valve (recycling background, fuelled atoms directly reaching the confined region, and recycled fuelling atoms) and the closed valve (background recycling only), as before against the temporally averaged particle flux. If the difference between open and closed valve would be too large, the density would increase too fast for agreement with interferometry. The grey line shows the flux of neutral

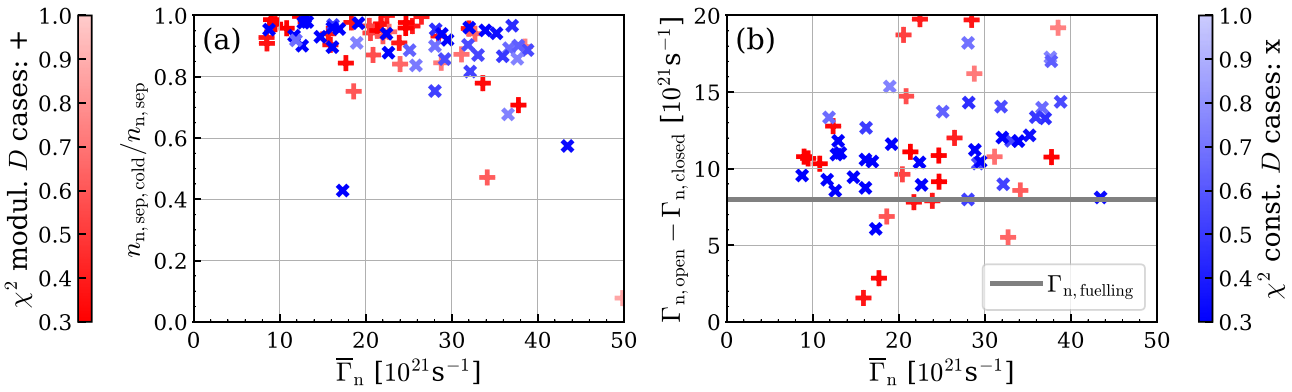

Figure 8. The share of 2 eV atoms of the neutral density at the separatrix (*a*) and the difference in particle flux across separatrix for open and closed valve (*b*), against the mean particle flux across the separatrix $\overline{\Gamma}_{\mathrm{n}}$. We also show the fuelling particle flux as grey line in (*b*). Simulations utilizing modulating D appear as red $+$, simulations with temporally constant D as blue $\times$. There are isolated simulations with $\chi^2 > 0.7$ outside of the shown areas.

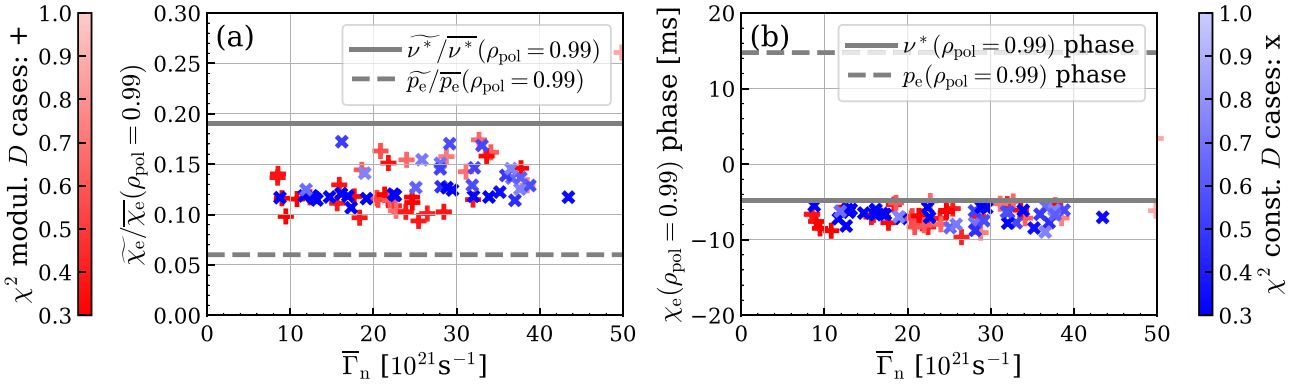

Figure 9. The relative modulation amplitude (*a*) and phase (*b*) of heat diffusivity (crosses), collisionality (solid grey line) and electron pressure (dashed grey line), against the mean particle flux across the separatrix $\overline{\Gamma}_{\mathrm{n}}$. Simulations utilizing modulating D appear as red $+$, simulations with temporally constant D as blue $\times$. There are isolated simulations with $\chi^2 > 0.7$ outside of the shown areas.

atoms that enter the vacuum vessel when the valve is open. ASTRA and the optimization procedure do not know about the fuelling particle flux. If recycling would not be influenced by the modulation and all fuelled deuterium atoms cross the separatrix all points should lie on the grey line. The difference in neutral particle flux lies above the fuelling particle flux for most simulations. This means that per fuelled atom more than one atom crosses the separatrix, possible because the additional recycling overcompensates losses such as ionization in the SOL.

Temporal evolution of transport. Unlike particle transport the heat transport depends only weakly on the source term. Together with the spatially resolved measurements of T_{e} this results in a considerably more accurate determination of χ_{e} than of D. In figure 10 we show the temporal evolution of χ_{e} at two radial positions and collisionality ν^*, as defined in [42], for one illustrating case. All three quantities modulate in phase. The temperature modulation at the edge and its propagation into the confined region is not only due to neutral effects and a change of n_{e}: transport, and thus the turbulence causing it, is increased by fuelling. In this work we focus on transport close to the separatrix at $\rho_{\mathrm{pol}} = 0.99$.

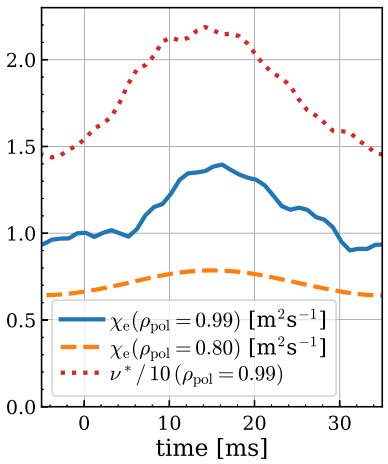

Figure 10. The heat diffusivity χ_{e} at $\rho_{\mathrm{pol}} = 0.99$ (blue, solid) and $\rho_{\mathrm{pol}} = 0.80$ (orange, dashed), and collisionality ν^* (red, dotted) at $\rho_{\mathrm{pol}} = 0.99$ as a function of time. We show the same case as in figure 6(*a*).

χ_{e} and ν^* modulate with similar phase and relative amplitude. Such a link between collisionality and turbulent transport is expected in several theoretical works [19–21]. This

is in line with experimental observations that an increase in fuelling, and therefore an increase in ν^*, does not lead to an as high increase in density as one would expect with constant D [10, 12]. To quantitatively investigate how the heat transport modulates we consider the relative modulation amplitude of $\chi_e(\rho_{pol} = 0.99)$ (figure 9(*a*)) and the phase of χ_e (figure 9(*b*)). We determine both quantities by fitting a sine to $\chi_e(\rho_{pol} = 0.99)$. The relative modulation amplitude of ν^* is $\pm 19\%$. The modulation amplitudes in successful simulations fall exclusively between $\pm 9\%$ and $\pm 18\%$. A linear dependency between χ_e and ν^*, as predicted for drift-Alfvén turbulence, would result in identical relative modulation amplitudes of $\pm 19\%$. This is just above the range of measured data, but we also neglected that the driving gradients decrease as transport increases, $\approx 8\%$ at the separatrix for n_e and $\approx 12\%$ at the separatrix for T_e. Qualitatively, the gradients at $\rho_{pol} = 0.99$ behave identically, but quantitatively they are less reliably measured. In figure 9(*b*) we show the phase of $\chi_e(\rho_{pol} = 0.99)$ and $\nu^*(\rho_{pol} = 0.99)$. Both quantities modulate with less than 5 ms difference in phase for all simulations, showing that transport and ν^* are strongly correlated. We also show the electron pressure p_e in figures 9(*a*) and (*b*). Pressure modulates with smaller relative amplitude than χ_e or ν^*, and in the opposite direction: the phases are shifted by half a period. We conclude that an increasing χ_e is strongly linked to an increasing ν^*. The minor differences in the phase could easily stem from other influencing quantities that modulate out of phase, e.g. the pressure gradient.

Experimental data suggests that D modulates in phase with χ_e: according to the lithium beam the density gradient at the separatrix flattens ≈ 10 ms after the valve is opened (figure 3(*c*)). The helium beam data shows more noise making the determination of the exact timing more difficult. Simultaneously, the interferometry shows a slowing of the density rise (figure 2(*b*)). Looking at χ_e in figure 10 we find that heat transport rises at the same time.

Note that modulation experiments offer an advantage over the analysis of steady state discharges with different fuelling levels when looking at the relative changes of χ_e: the transported power depends not only at χ_e and ∇T_e but also on n_e. Uncertainties of n_e therefore influence the accuracy of χ_e. But constant errors in n_e cancel when we calculate the relative changes of χ_e. By modulating instead of comparing different phases or even discharges the conditions change less, keeping more of the errors of the density profile constant and thus without effect.

6. Conclusions

We performed fuelling modulation experiments at the AUG tokamak in an L-mode plasma to study the edge particle transport. Current core particle transport studies involve more discharges that better cover various plasma conditions [9]. Our smaller study is still highly relevant because edge particle transport is far less understood than core particle transport:

(a) Faster time scales and shorter length scales have to be resolved experimentally. One example of this are detrimental SOL effects on reflectometry that disturb the reconstruction of profiles. These effects, among others, forced us to discard reflectometry data which has proven to be highly valuable for core transport studies [9]. Similarly we cannot rely on Thomson spectroscopy as the time scales considered cannot be resolved. Instead we analyse data from various diagnostics, e.g. ECE, interferometry, thermal helium beam spectroscopy, lithium beam spectroscopy, in an integrated data approach to nevertheless arrive at our conclusions.

(b) The (flux surfaced averaged) neutral particle source in the plasma edge is notoriously difficult to quantify, already in steady state but even more so in dynamic situations which are required to disentangle diffusion and pinch. We still are able to draw conclusions about the particle transport despite these additional hindrances compared to core transport.

(c) Gas puff modulation studies performed for particle transport studies usually assume that transport itself is not perturbed by the modulation. We show that, at least in the edge, this is in general not a valid assumption.

We modulate the deuterium gas flow into the torus. When the gas flow increases the separatrix cools and increases in density. The cooling propagates as cold pulse into the core plasma. Interferometry measures a density increase inside the separatrix. The density profile at the separatrix flattens, suggesting an increase in transport.

By modelling the discharge in ASTRA we characterized the solution set of parameters, and thus were able to determine transport coefficients and properties concerning fuelling and edge turbulence. The well resolved measurements of n_e and T_e from the lithium and thermal helium beams were essential for the analysis.

The experimental data allows for a range of particle diffusivities and pinch velocities in the region outside of $\rho_{pol} = 0.95$: most simulations lie within $\overline{D} = (0.20 \pm 0.13)\ \mathrm{m^2\ s^{-1}}$ and $v = (-1 \pm 2)\ \mathrm{m\ s^{-1}}$. A pinch is not necessary to explain the measured data. We quantified the relative modulation amplitude of χ_e, which is between $\pm 9\%$ and $\pm 18\%$. High heat diffusivity correlates with high collisionality ν^*, as predicted by several works [19–21]. Experimental data suggests that particle transport modulates in phase with ν^* and χ_e. On average, each fuelled atom crosses the separatrix more than once due to recycling. The source profile is narrow, such as if most neutrals cross the separatrix with Franck–Condon energies or at a location with large flux expansion in the vicinity of the X-point.

The presented method will be used to analyse more L-mode plasmas with variations in shape, density and heating as well as other plasma scenarios in H-mode. We also want to extend our method of gas puff modulation and ASTRA modelling by incorporating measurements of neutral atoms fuelling the plasma.

Acknowledgments

We want to thank Matthias Willensdorfer for fruitful discussions and Daniel Wendler and Diego José Cruz Zabala for help with the experiment. This work has been carried out within the framework of the EUROfusion Consortium and has received funding from the Euratom Research and Training Programme 2014–2018 and 2019–2020 under Grant Agreement No. 633053. The views and opinions expressed herein do not necessarily reflect those of the European Commission.

ORCID iDs

C.U. Schuster https://orcid.org/0000-0002-6695-3336
E. Wolfrum https://orcid.org/0000-0002-6645-6882
E. Fable https://orcid.org/0000-0001-5019-9685
M. Griener https://orcid.org/0000-0003-2953-536X
C. Angioni https://orcid.org/0000-0003-0270-9630
T. Eich https://orcid.org/0000-0003-3065-8420
P. Manz https://orcid.org/0000-0002-5724-0174
U. Stroth https://orcid.org/0000-0003-1104-2233

References

[1] Luda T. *et al* (EUROfusion MST1 Team) 2020 Integrated modeling of ASDEX Upgrade plasmas combining core, pedestal and scrape-off layer physics *Nucl. Fusion* **60** 036023
[2] Snyder P.B., Groebner R.J., Hughes J.W., Osborne T.H., Beurskens M., Leonard A.W., Wilson H.R. and Xu X.Q. 2011 A first-principles predictive model of the pedestal height and width: development, testing and ITER optimization with the EPED model *Nucl. Fusion* **51** 103016
[3] Ida K. *et al* 2020 Transition between isotope-mixing and non-mixing states in hydrogen–deuterium mixture plasmas *Phys. Rev. Lett.* **124** 025002
[4] Gentle K.W., Gehre O. and Krieger K. 1992 Determination of particle transport coefficients in ASDEX by gas modulation *Nucl. Fusion* **32** 217
[5] Kramer G.J. (ACC Sips) 1993 Analysis of reflectometry density profile measurements in jet *Plasma Phys. Control. Fusion* **35** 743
[6] Baker D.R. *et al* (DIII-D Team) 1998 Measurement of electron particle transport coefficients in different operational modes of DIII-D *Nucl. Fusion* **38** 485
[7] Koponen J.P.T. *et al* (ECH Group) 2000 Perturbative particle transport studies in the W7-as stellarator *Nucl. Fusion* **40** 365
[8] Tanaka K. *et al* 2005 Experimental study of particle transport and density fluctuations in LHD *Nucl. Fusion* **46** 110
[9] Tala T. *et al* 2019 Density peaking in JET-determined by fuelling or transport? *Nucl. Fusion* **59** 126030
[10] Mordijck S. 2020 Overview of density pedestal structure: role of fueling versus transport *Nucl. Fusion* **60** 082006
[11] Groebner R.J., Mahdavi M.A., Leonard A.W., Osborne T.H., Porter G.D., Colchin R.J. and Owen L.W. 2002 The role of neutrals in high-mode (H-mode) pedestal formation *Phys. Plasmas* **9** 2134–40
[12] Hughes J.W., LaBombard B., Terry J., Hubbard A. and Lipschultz B. 2007 Edge profile stiffness and insensitivity of the density pedestal to neutral fuelling in Alcator C-Mod edge transport barriers *Nucl. Fusion* **47** 1057
[13] Schneider P.A. *et al* 2012 Differences in the H-mode pedestal width of temperature and density *Plasma Phys. Control. Fusion* **54** 105009
[14] Willensdorfer M. *et al* 2013 Particle transport analysis of the density build-up after the L–H transition in ASDEX Upgrade *Nucl. Fusion* **53** 093020
[15] Griener M. *et al* 2017 Fast piezoelectric valve offering controlled gas injection in magnetically confined fusion plasmas for diagnostic and fuelling purposes *Rev. Sci. Instrum.* **88** 033509
[16] Pereverzev G. and Yushmanov P.N. 2002 *ASTRA Automated System for Transport Analysis in a Tokamak* 5/98 Max-Planck-Institute for Plasma Physics Garching
[17] Fable E. *et al* 2013 Novel free-boundary equilibrium and transport solver with theory-based models and its validation against ASDEX Upgrade current ramp scenarios *Plasma Phys. Control. Fusion* **55** 124028
[18] Fable E., Angioni C., Ivanov A.A., Lackner K., Maj O., Yu S., Medvedev G, Pautasso G. and Pereverzev G.V. 2013 A stable scheme for computation of coupled transport and equilibrium equations in tokamaks *Nucl. Fusion* **53** 033002
[19] Bonanomi N. *et al* (EUROFusion MST1 Team) 2019 Effect of the isotope mass on the turbulent transport at the edge of l-mode plasmas in ASDEX Upgrade and JET-ILW *Nucl. Fusion* **59** 126025
[20] Bourdelle C., Garbet X., Singh R. and Schmitz L. 2012 New glance at resistive ballooning modes at the edge of tokamak plasmas *Plasma Phys. Control. Fusion* **54** 115003
[21] Rogers B.N., Drake J.F. and Zeiler A. 1998 Phase space of tokamak edge turbulence, the L–H transition, and the formation of the edge pedestal *Phys. Rev. Lett.* **81** 4396–9
[22] Scott B.D. 2007 Tokamak edge turbulence: background theory and computation *Plasma Phys. Control. Fusion* **49** S25
[23] McCarthy D.R., Guzdar P.N., Drake J.F., Antonsen T.M. Jr and Hassam A.B. 1992 Stability of resistive and ideal ballooning modes in the Texas experimental tokamak and DIII-D *Phys. Fluids* B **4** 1846–54
[24] Meyer H. *et al* 2019 Overview of physics studies on ASDEX Upgrade *Nucl. Fusion* **59** 112014
[25] David P., Bernert M., Pütterich T., Fuchs C., Glöggler S. and Eich T. (the ASDEX Upgrade Team) 2021 Optimization of the computation of total and local radiated power at ASDEX Upgrade *Nucl. Fusion* **61** 066025
[26] Mlynek A., Schramm G., Eixenberger H., Sips G., ,McCormick K., Zilker M., Behler K. and Eheberg J. (ASDEX Upgrade Team) 2010 Design of a digital multiradian phase detector and its application in fusion plasma interferometry *Rev. Sci. Instrum.* **81** 033507
[27] Wolfrum E., Aumayr F., Wutte D., Winter H., Hintz E., Rusbüldt D. and Schorn R.P. 1993 Fast lithium-beam spectroscopy of tokamak edge plasmas *Rev. Sci. Instrum.* **64** 2285–92
[28] Fischer R. *et al* 2008 Probabilistic lithium beam data analysis *Plasma Phys. Control. Fusion* **50** 085009
[29] Griener M. *et al* (ASDEX Upgrade Team) 2018 Helium line ratio spectroscopy for high spatiotemporal resolution plasma edge profile measurements at ASDEX Upgrade *Rev. Sci. Instrum.* **89** 10D102
[30] Wendler D. *et al* 2022 Collisional radiative model for the evaluation of the thermal helium beam diagnostic at ASDEX Upgrade *Plasma Phys. Control. Fusion* **64** 045004
[31] Naulin V. 2007 Turbulent transport and the plasma edge *J. Nucl. Mater.* **363–365** 24–31
[32] Boedo J.A. *et al* 2003 Transport by intermittency in the boundary of the DIII-D tokamak *Phys. Plasmas* **10** 1670–7
[33] Nold B., Conway G.D., Happel T., Müller H.W., Ramisch M., Rohde V. and Stroth U. 2010 Generation of blobs and holes in the edge of the ASDEX Upgrade tokamak *Plasma Phys. Control. Fusion* **52** 065005
[34] D'ippolito D.A., Myra J.R. and Zweben S.J. 2011 Convective transport by intermittent blob-filaments: comparison of theory and experiment *Phys. Plasmas* **18** 060501

[35] Vianello N. *et al* 2019 Scrape-off layer transport and filament characteristics in high-density tokamak regimes *Nucl. Fusion* **60** 016001
[36] Manz P. *et al* 2020 The diffusion limit of ballistic transport in the scrape-off layer *Phys. Plasmas* **27** 022506
[37] Marandet Y. *et al* 2011 Transport of neutral particles in turbulent scrape-off layer plasmas *Nucl. Fusion* **51** 083035
[38] Moore D.S. 1976 *Chi-Square Tests* 469 Purdue University, Department of Statistics
[39] Fischer R., Fuchs C.J., Kurzan B., Suttrop W. and Wolfrum E. (ASDEX Upgrade Team) 2010 Integrated data analysis of profile diagnostics at ASDEX Upgrade *Fusion Sci. Technol.* **58** 675–84
[40] Virtanen P. *et al* 2020 SciPy 1.0: fundamental algorithms for scientific computing in Python *Nat. Methods* **17** 261–72
[41] Guthrie W.F. 2020 1. Exploratory Data Aalysis *NIST/SEMATECH e-Handbook of Statistical Methods (NIST Handbook 151)* (Gaithersburg, MA: NIST National Institute of Standards and Technology) (https://doi.org/10.18434/M32189)
[42] Oyama N. *et al* 2006 Pedestal conditions for small ELM regimes in tokamaks *Plasma Phys. Control. Fusion* **48** A171